Structural Durability & Health Monitoring

Tech Science Press

https://doi.org/10.32604/sdhm.2026.079754

ARTICLE

Check for updates

Non-Contact Testing of Concrete Stress via the Laser-Generated Rayleigh Wave

Mengxue Li[1,2], **Xinyi Chen**[1,*] **and Yuxi Xie**[2]

[1]State Key Laboratory of Mountain Bridge and Tunnel Engineering, Chongqing Jiaotong University, Chongqing, China
[2]Chongqing Institute of Urban Governance, Chongqing, China

*Corresponding Author: Xinyi Chen. Email: cxy@mails.cqjtu.edu.cn

Received: 27 January 2026; Accepted: 26 March 2026; Published: 24 August 2026

Highlights

- The correlation between concrete stress and R-wave velocity was clarified.
- Concrete stress was evaluated using the measured R-wave velocity.
- The proposed method is non-contact and suitable for in-service structures.

ABSTRACT: Concrete stress is a critical indicator for evaluating the performance of concrete structures. To achieve non-contact testing of concrete stress, this study analyzed the propagation of laser-generated Rayleigh waves (R-wave) in concrete. A correlation model was established between the concrete stress and the R-wave velocity. To validate the theoretical analysis, ultrasonic experiments were conducted. The experimental results demonstrated that the stress history of concrete determines whether a stable linear relationship exists between the stress and the R-wave velocity. Additionally, the acoustoelastic coefficient of concrete was found to vary with its age. Based on these findings, a concrete stress evaluation method based on the R-wave velocity was proposed. When the stress was less than or greater than 16 MPa, the testing error was less than 8 or 2 MPa, respectively. Theoretical and experimental results demonstrated the feasibility of the proposed method, providing a promising solution for the non-contact stress testing of in-service concrete structures.

KEYWORDS: Concrete stress; non-contact testing; laser-ultrasonic; Rayleigh wave; acoustoelastic effect

1 Introduction

1.1 Motivation

Concrete, characterized by its low cost and ease of acquisition, is widely used in infrastructure, such as bridges, dams, and buildings. Subject to loads and environmental factors, the performance of concrete deteriorates, compromising structural strength and safety [1]. Besides, as structures age, they may not be able to withstand increasing demands. As a result, there is an increasing need to reinforce or extend in-service structures [2]. Such reinforcement and extension require an accurate assessment of the structural performance [3]. Since concrete stress is a critical indicator for evaluating the performance of concrete structures [4], researchers have proposed concrete stress testing methods based on different principles.

1.2 Literature Review

Existing concrete stress testing methods fall into two categories: destructive and non-destructive. Destructive testing methods include the hole drilling method, the core drilling method [5], and the grooving method. These methods offer high accuracy. However, they inevitably damage the concrete, leading to stress concentration and redistribution [6]. As a result, the application of destructive testing methods is limited.

Non-destructive testing methods for concrete stress are primarily based on the acoustic emission phenomenon, the nonlinear ultrasonic wave theory [7], the ultrasonic coda wave theory, and the acoustoelastic effect. The acoustic emission method is a passive testing method, particularly suited for monitoring stress variations [8]. This method evaluates concrete stress by observing the elastic waves generated by stress release. The correlation between stress and acoustic emission signals is influenced by material properties and loading patterns. Thus, for the acoustic emission method, establishing an accurate correlation model is challenging. Additionally, the acoustic emission method is highly sensitive. Stress, microcracks, and environmental vibrations can trigger acoustic emissions. To enhance testing accuracy, machine learning algorithms can be employed for signal processing and stress evaluation.

The nonlinear ultrasonic wave method uses the nonlinear effects that are generated during wave propagation to identify microdamage and stress variations. Compared to traditional linear ultrasonic methods, the nonlinear ultrasonic method is more sensitive to minor stress variations. Research on nonlinear ultrasonic testing of concrete stress focuses on three aspects: nonlinear ultrasonic signal acquisition, signal processing and feature extraction, and stress evaluation based on nonlinear characteristics [9]. These three issues have been partially addressed. The nonlinear ultrasonic wave method has been applied to concrete stress testing. However, due to its high sensitivity, the nonlinear ultrasonic method's ability to resist interference needs improvement [10].

The coda wave method identifies stress variations by analyzing changes in coda waves resulting from multiple scattering. Like the nonlinear ultrasonic wave method, the coda wave method can identify minor stress variations. The coda wave method has minimal testing environment requirements and good adaptability. Therefore, it has been applied in practical engineering. However, coda waves are susceptible to concrete heterogeneity. Factors such as aggregate distribution, voids, and cracks can influence the propagation of the coda wave. With the expansion of microcracks, the testing accuracy of the coda wave method decreases rapidly [11]. Consequently, the coda wave method is better suited for testing low-stress concrete.

The acoustoelastic effect demonstrates the correlation between the applied stress and the velocity of elastic waves in solids [12]. Stress testing methods based on the acoustoelastic effect have been applied to steel, concrete, and orthotropic materials. Traditionally, these methods rely on longitudinal waves and shear waves [13]. These waves are typically generated and collected by piezoelectric transducers [14], which are difficult to install on curved surfaces. Additionally, the performance of the coupling agents, used to transmit waves from transducers to concrete, is influenced by environmental conditions [15]. In practice, selecting suitable coupling agents is challenging.

To overcome the limitations of the stress testing methods based on the acoustoelastic effect, laser ultrasonic technology [16] has been employed. Laser-generated Rayleigh waves (R-wave) are generated by irradiating a non-piezoelectric body. The laser-ultrasonic technology enables non-contact excitation and collection [17]. This approach eliminates the need for coupling agents, making it suitable for harsh environments and complex structures. Unlike piezoelectric transducers, the shape and size of the laser can be adjusted to ensure high spatial resolution and accuracy [18]. Although research on concrete stress testing via R-waves has been conducted, most studies focus on piezoelectric transducers [19]. Systematic investigations of concrete stress testing based on the laser-generated R-wave are lacking. Achieving non-contact testing of concrete stress remains challenging. In view of this, this study investigates the non-contact testing of concrete stress via the laser-generated R-wave.

1.3 Contribution

In this paper, the propagation of R-waves in concrete and the acoustoelastic effect under uniaxial stress were analyzed. Ultrasonic experiments were conducted. The influence of concrete properties, stress, stress history, and concrete age on the R-wave was clarified. A concrete stress evaluation method was proposed and verified. The main contributions of this paper to the published literature are summarized as follows:

(1) Concrete stress testing based on the acoustoelastic effect employs piezoelectric transducers to generate and collect ultrasonic waves. However, these transducers require high surface flatness of the test object and offer limited spatial resolution due to their physical dimensions [20]. To overcome these limitations, this study employed laser ultrasonic technology to generate and collect R-waves. A stress testing method via the laser-generated R-wave was proposed, achieving non-contact testing of concrete stress. The proposed method is suitable for curved surfaces and achieves a millimeter-scale spatial resolution. As a result, the applicability and accuracy of the stress testing based on the acoustoelastic effect are enhanced.

(2) Stress testing methods based on the acoustoelastic effect rely on longitudinal waves and shear waves [21]. However, the application of bulk wave-based testing is not optimal for large-volume concrete structures [22]. Given this, the propagation of R-waves in concrete and the acoustoelastic effect under uniaxial stress were analyzed. A concrete stress evaluation method based on the measured R-wave velocity was proposed. As a surface wave, the stress testing via the laser-generated R-wave enables single-sided testing. Thus, the applicability of the stress testing based on the acoustoelastic effect extends from small-volume to large-volume concrete structures.

1.4 Organization of the Paper

The rest of this paper is organized as follows: Section 2 analyzes the propagation of R-waves in concrete and derives the correlation between the concrete stress and the R-wave velocity. Section 3 details the design of ultrasonic experiments for concrete stress testing. Section 4 discusses the influence of concrete properties, stress, stress history, and concrete age on the R-wave. A concrete stress evaluation method is proposed and verified.

2 Theory Background

Concrete is generally subjected to uniaxial stress, under which the acoustoelastic effect of the plane stress state can be expressed as Eq. (1) [23]. In Eq. (1), V_{R} is the R-wave velocity, V_{R0} is the R-wave velocity when free from stress, C_{R} is the acoustoelastic coefficient, and σ is the uniaxial stress.

$$(V_{\mathrm{R}} - V_{\mathrm{R0}})/V_{\mathrm{R0}} = C_{\mathrm{R}}\sigma \tag{1}$$

The R-wave velocity is determined by the time of flight (TOF) and the propagation distance. For determined testing points, the TOF is influenced by the propagation medium and the actual propagation distance. Concrete is a heterogeneous material composed of gravel, sand, and cement. Considering sand and cement as a whole (cement mortar), concrete is composed of gravel and cement mortar. The R-wave velocity in gravel differs from that in cement mortar [24]. This discrepancy can be expressed as Eq. (2), where V_{Rg} is the R-wave velocity in gravel, V_{Rcm} is the R-wave velocity in cement mortar, and α is a constant.

$$V_{\mathrm{Rg}} = \alpha V_{\mathrm{Rcm}} \tag{2}$$

As shown in Fig. 1, the gravel is randomly distributed within the concrete. Along different paths, the proportion of gravel varies, resulting in discrepancies between the calculated R-wave velocities and the actual

R-wave velocities. As expressed in Eq. (3), this variation in the propagation medium can be converted into a change in the propagation distance. In Eq. (3), s is the propagation distance, Δs_{pm} is the distance increment caused by the variation in the medium, and β is the proportion of gravel along the propagation path.

$$\Delta s_{\mathrm{pm}} = \left(\frac{\beta s}{\alpha V_{\mathrm{Rcm}}} + \frac{(1-\beta)\, s}{V_{\mathrm{Rcm}}}\right) V_{\mathrm{Rcm}} - s = \left(1 + \frac{1}{\alpha}\right) \beta s \tag{3}$$

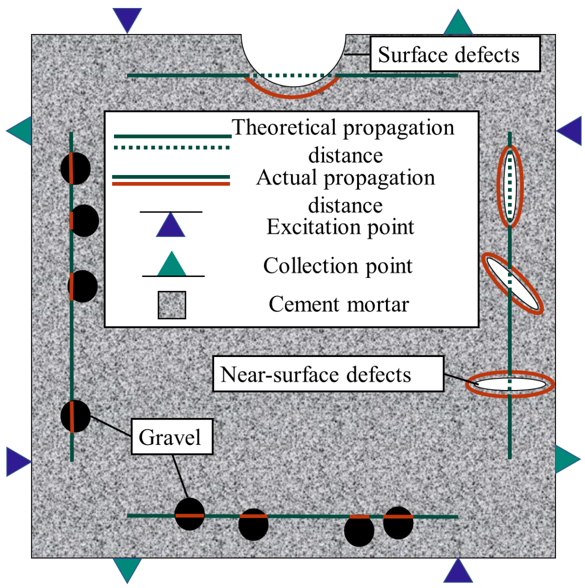

Figure 1: Propagation of R-waves in concrete.

Defects that affect R-waves can be categorized into surface defects and near-surface defects. When a load is applied, existing defects tend to develop. As illustrated in Fig. 1, the surface defects cause wave scattering, thereby increasing the wave propagation distance. The influence of the near-surface defects on the propagation distance is expressed in Eq. (4). In Eq. (4), Δs_{nsd} is the distance increment caused by the near-surface defects, n is the number of the near-surface defects, i is the index of the near-surface defect, $s_{\mathrm{nsd}i}$ is the theoretical propagation distance of the i-th defect, γ_i is the ratio of the actual to theoretical propagation distance of the i-th defect, f is the magnification factor function, and σ_{his} is the stress history.

$$\Delta s_{\mathrm{nsd}} = \left[\sum_{i=1}^{n} (\gamma_i - 1)\, s_{\mathrm{nsd}i}\right] \mathrm{f}\,(\sigma, \sigma_{\mathrm{his}}) \tag{4}$$

Similarly, the influence of surface defects on the propagation distance can be expressed as Eq. (5), where Δs_{sd} is the distance increment caused by the surface defects, m is the number of the surface defects, j is the index of the surface defect, $s_{\mathrm{sd}j}$ is the theoretical propagation distance of the j-th defect, η_j is the ratio of the actual to theoretical propagation distance of the j-th defect, and g is the magnification factor function.

$$\Delta s_{\mathrm{sd}} = \left[\sum_{j=1}^{m} (\eta_i - 1)\, s_{\mathrm{sd}j}\right] \mathrm{g}\,(\sigma, \sigma_{\mathrm{his}}) \tag{5}$$

According to the acoustoelastic theory, the wave velocity is influenced by the material stress. When the propagation distance remains constant, variations in the wave velocity are reflected in the TOF. In concrete, the actual propagation distance increases when the R-wave travels along the surface of the defects. To integrate the effects of stress and defects, it is assumed that the intrinsic wave velocity and the propagation distance remain constant. Thus, the change in the intrinsic wave velocity caused by stress can be equated to an increase in the actual propagation distance. Under this assumption, the combined effects of stress and defects influence the TOF of the R-wave, resulting in variations in the measured R-wave velocity. In the following discussion, the term "R-wave velocity" refers to the measured R-wave velocity.

By combining Eqs. (1) and (3)–(5), the propagation of R-waves in concrete can be expressed as Eq. (6), where V_{RT} is the measured R-wave velocity. For in-service structures showing the Kaiser effect [25], the Δs_{nsd}, Δs_{sd}, f, and g are constants. For a determined propagation path, s, Δs_{pm}, and V_{Rcm} are constants. Subsequently, Eq. (6) can be further simplified, where V_{RT0} is the V_{RT} measured free from stress. Eq. (6) indicates that once the acoustoelastic coefficient of the R-wave is determined, the concrete stress can be evaluated based on the measured R-wave velocity.

$$V_{RT} = \frac{s\left(C_R \cdot \sigma + 1\right)}{s + \Delta s_{pm} + \Delta s_{nsd} \cdot \mathrm{f}\left(\sigma, \sigma_{his}\right) + \Delta s_{sd} \cdot \mathrm{g}\left(\sigma, \sigma_{his}\right)} V_{Rcm} \Rightarrow \frac{V_{RT} - V_{RT0}}{V_{RT0}} = C_R \sigma \tag{6}$$

3 Experimental Method

Concrete is a heterogeneous material whose physical properties are variable. To validate the theoretical analysis, ultrasonic experiments on concrete stress testing were conducted.

3.1 Material Properties

In this experiment, the concrete was composed of Portland cement, sand, gravel, water, and a water-reducing agent. The Portland cement was grade PI 42.5. The content of active admixtures in the cement was between 5% and 20%, while the content of inert admixtures was less than 5%. The sand had a fineness modulus of 2.76 and particle sizes smaller than 4.75 mm. The gravel was a mixture of three types with a ratio of 2:5:3. The particle sizes of these three types of gravel were 5–10 mm, 10–20 mm, and 20–31.5 mm, respectively. The mass of the Polycarboxylic water reducer was 0.9% of the cement mass. As shown in Table 1, this experiment employed a single concrete mix design with an anticipated concrete strength of 40 MPa. The aim was to ensure similar physical properties among all specimens.

Table 1: Concrete mix design (kg/m^3).

Cement	Sand	Gravel	Water	Water-Reducing Agent
370	756	1136	160	3.33

3.2 Specimens and Loading Procedures

Thirty-six cubic specimens, each measuring 150 mm × 150 mm × 150 mm, were prepared. After casting, the specimens were cured in the laboratory for 36 h before being demolded. The R-wave velocity exhibits lesser variation with concrete age when the concrete is older than 15 days [26]. To investigate the R-wave propagation in concrete older than 28 days, the specimens were cured for 28, 56, and 84 days, respectively. As shown in Table 2, the specimens were labeled according to their curing time and loading procedures.

To determine the compressive strength and Young's modulus of the concrete, Group 1 was loaded to failure at a rate of 0.5 MPa/s. Group 2 remained unstressed, and ultrasonic tests were conducted to evaluate the influence of the propagation medium and initial defects on the R-wave velocity. The specimen surfaces in contact with the side formwork were labeled as S1, S2, S3, and S4. Each surface had eight testing paths that were free of surface defects. As shown in Fig. 2, the testing paths radiated from the surface center at 45-degree intervals. The testing paths were labeled based on the clockwise angle from the reference path. The reference path on surface S1 of specimen B28-1 was labeled as B28-1-S1-0. With the collection point fixed at the surface center, the excitation point moved along the paths. The propagation distance increased from 15 to 35 mm with a step of 5 mm. At each step, the R-wave signal was collected 36 times. Based on the propagation distance and the measured TOF, the R-wave velocity was calculated.

Table 2: Label of the specimens used in the experiment.

Group	Label	Loading Procedure	Ultrasonic Test	Measured Characteristic
1	A28-1~A28-10	Loading to failure	No	Concrete Properties
2	B28-1/2	Free from stress	Yes	R-wave velocity
3	C28/56/84-12-1/2	Cyclic load (Max stress = 12 MPa) & Loading to failure	Yes	R-wave velocity
4	C28/56/84-18-1/2	Cyclic load (Max stress = 18 MPa) & Loading to failure	Yes	R-wave velocity
5	C28/56/84-28-1/2	Cyclic load (Max stress = 28 MPa) & Loading to failure	Yes	R-wave velocity
6	D28/56/84-1/2	Loading to failure	Yes	R-wave velocity

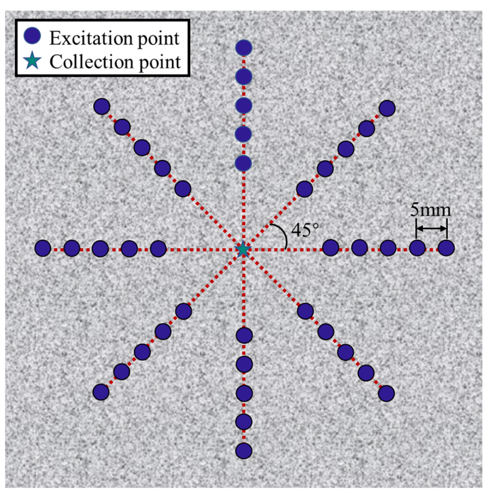

Figure 2: Testing paths on the surface of the specimens of Group 2.

Groups 3, 4, and 5 were subjected to cyclic loads with different maximum stresses. Preliminary studies indicated that the physical properties of the concrete specimens stabilized after four load cycles. Therefore, in this experiment, the cyclic load consisted of six load cycles. The application of the cyclic loads served two objectives. The first was to validate the correlation between the concrete stress and the R-wave velocity, as expressed in Eq. (6). The second was to clarify the influence of the stress history on the R-wave velocity. The cyclic loads were applied using a universal testing machine. As shown in Fig. 3, after six load cycles, the specimen was compressed to failure. For ease of comparison, this final loading procedure was denoted as Cycle 7. The loading step was 2 MPa, and the loading speed was 0.5 kN/s. At each stress level, the stress was maintained for 165 s, during which the R-wave signal was collected 36 times.

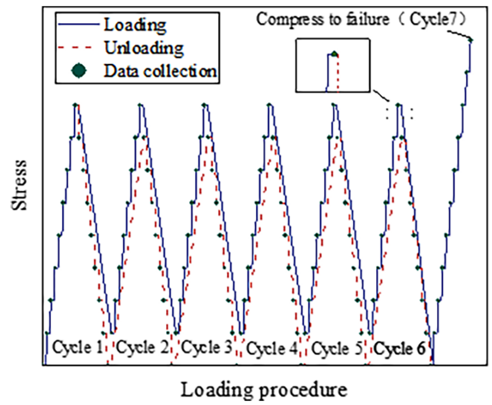

Figure 3: Loading procedure of Group 3, Group 4, and Group 5.

3.3 Experimental System Based on the Laser-Generated R-Wave

To conduct the ultrasonic tests, an experimental system based on the laser-generated R-wave was established. As shown in Fig. 4, the experimental system consisted of a pulsed laser, a lens, a laser vibrometer, an oscilloscope, a computer, and a universal testing machine. The Q-switched Nd: YAG pulsed laser generated an R-wave at the excitation point. The pulsed laser had a wavelength of 1064 nm and a pulse width of 1.5 ns. The excitation frequency was set at 1 Hz, and its peak current was 100 A. The R-wave was generated through the ablation mechanism, which resulted in negligible micron-scale damage to the concrete. To enhance the intensity of the incident laser beam, a plano-convex lens with a focal length of 125 mm was attached to the pulsed laser.

The R-wave was collected by the modular vibrometer, which had a frequency bandwidth of up to 24 MHz and a vibration speed range of ±25 m/s. The laser spot diameter was on the micrometer scale. The oscilloscope, which had a bandwidth of 200 MHz and a maximum sampling rate of 2 GS/s, was used to visualize the R-wave. The frequency of the signal acquisition was 1 Hz. After filtering out low-frequency noise, the signal was transformed into a discrete signal comprising 2500 data points. Then, the R-wave data were stored in the computer.

As shown in Fig. 4, to enhance the signal-to-noise ratio of the measured signal, the vibrometer was positioned 30 mm from the specimen. The collection laser provided by the vibrometer was perpendicular to the specimen surface and converged at the surface center. The pulsed laser was positioned 125 mm from the specimen surface to match the focal length of the lens. To prevent interference between the vibrometer and the pulsed laser, the excitation laser was set to an incident angle of 15 degrees. The distance between the excitation point and the collection point was 10 mm, and the connection line was parallel to the compressive stress. This configuration was implemented to ensure the optimal sensitivity of the R-wave velocity to stress variations.

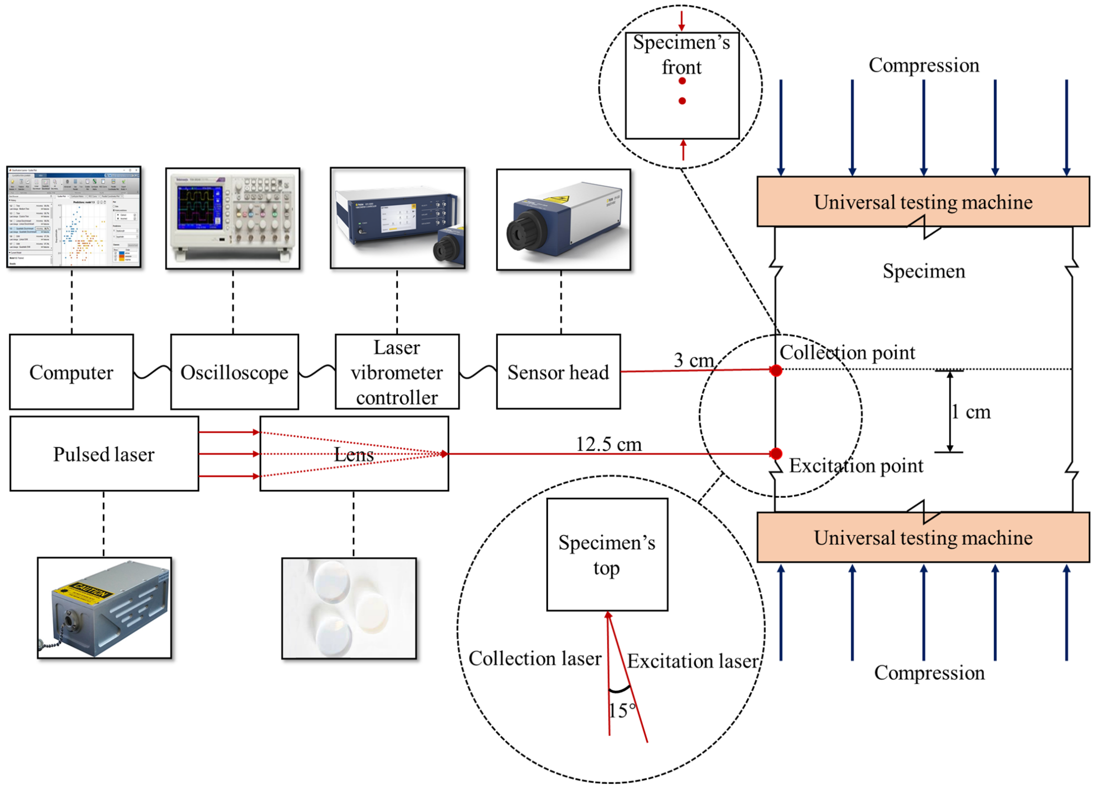

Figure 4: Experimental system based on the laser-generated R-wave.

3.4 Signal Processing

To minimize random errors, the collected discrete signals were averaged. The signal collected before the application of the load was designated as the reference signal, and the signals collected at different stress levels served as the comparison signals. These discrete signals can be expressed as Eq. (7), where h (equal to 2500) is the number of signal sampling points, S_{refc} is the continuous reference signal, S_{refd} is the discrete reference signal, S_{comc} is the continuous comparison signal, S_{comd} is the discrete comparison signal, T is the time interval between two sample points, and δ is the impulse function.

$$S_{\text{refd}}(k) = \sum_{k=1}^{h} S_{\text{refc}}(t) \cdot \delta(t - kT)$$

$$S_{\text{comd}}(\text{k}) = \sum_{k=1}^{h} S_{\text{comc}}(t) \cdot \delta(t - kT) \quad (7)$$

The two discrete signals were denoised using the wavelet transform [27]. For the wavelet denoising, the threshold selection rule employed a heuristic variant of Stein's unbiased risk with soft thresholding. The threshold was not rescaled. Additionally, the wavelet decomposition was performed at five levels using the sym4 wavelet basis function. After denoising, the delay between the two signals was calculated using the cross-correlation method [28], which can be expressed as Eq. (8). In Eq. (8), Δk is the artificially added signal delay, which increases from $-h+1$ to $h-1$. The delay between the two signals is determined when the maximum value of $R(\Delta k)$ is achieved. This delay can be expressed as Eq. (9), where Δk_{Rmax} is the Δk when $R(\Delta k)$ reaches its maximum, and ΔT is the delay in the TOF between the comparison and reference signals. In this study, the signal measurement duration of the oscilloscope was set to 25 μs. Thus, the resolution of the ΔT was 0.01 μs, which was equal to the time interval between two sampling points. Once the TOF of the R-wave was determined, the R-wave velocity could be calculated using the propagation distance.

$$R(\Delta k) = \left| \frac{1}{h} \sum_{k=1}^{h} \left[S_{\text{refd}}(k) \cdot S_{\text{comd}}(k + \Delta k) \right] \right| \tag{8}$$

$$\Delta T = T \cdot \Delta k_{\text{Rmax}} \tag{9}$$

4 Results and Discussion

4.1 Concrete Properties of the Specimens

After measuring the dimensions and density, Group 1 was tested according to ISO 1920-4:2020 to determine the concrete's compressive strength and Young's modulus. The average physical properties of these ten specimens were taken as the representative values. As shown in Table 3, the specimens' length and width exceeded the theoretical values due to the limited rigidity of the plastic formwork. The compressive strength was higher than the theoretical value. Both the compressive strength and the Young's modulus met the requirements for the designed loading procedures.

Table 3: Dimensions and physical properties of the specimens.

Label	Length (mm)	Width (mm)	Height (mm)	Density (kg/m^3)	Young's Modulus (GPa)	Compressive Strength (MPa)
Theoretical value	150.00	150.00	150.00	2425.33	32.50	40.00
Average value	150.46	150.33	152.05	2432.59	35.16	45.11
Standard deviation	0.32	0.24	0.62	31.75	1.44	1.62

4.2 Influence of Concrete Properties on the R-Wave Velocity

Specimens B28-1 and B28-2, which were free from stress, were tested to obtain the R-wave velocity along different paths. As shown in Fig. 5a, as the propagation distance increased, the R-wave's TOF increased while its amplitude decreased. To analyze the relationship between the TOF and the propagation distance, the TOF increment was calculated.

As shown in Fig. 5b, the maximum standard deviation of the TOF increment was 0.024 μs, indicating the stability of the R-wave signals. This also demonstrated that averaging the 36 collected R-wave signals yielded an accurate R-wave signal. The R-wave velocity was determined by dividing the propagation distance increment by the TOF increment. Along a specific propagation path, the R-wave velocities corresponding to different excitation points exhibited minor variations. Similarly, on a specific surface, the R-wave velocities corresponding to different propagation paths also showed variations. These variations were attributed to the differences in the propagation medium and near-surface defects. As shown in Fig. 5b, a strong linear relationship was observed between TOF and propagation distance. Linear fitting was performed to obtain the slope of the TOF-propagation distance relationship, and this slope was considered the R-wave velocity. As shown in Fig. 6, the R-wave velocities of specimens B28-1 and B28-2 ranged from 3370.2 to 3634.2 m/s. This indicates that the concrete specimens with the same mix design have similar R-wave velocities.

On one surface, the R-wave velocities corresponding to different propagation paths varied. The range of variation was minimal on surface B28-2-S2 (48.60 m/s) and maximal on surface B28-2-S4 (78.70 m/s). The standard deviation across all surfaces was 24.45 m/s, which corresponded to 0.67%–0.73% of the average R-wave velocity. Since there were no surface defects on the propagation paths, these differences were attributed to the near-surface defects and the propagation medium. Since the paths on one surface had a similar casting environment, the variation in R-wave velocities was minimal.

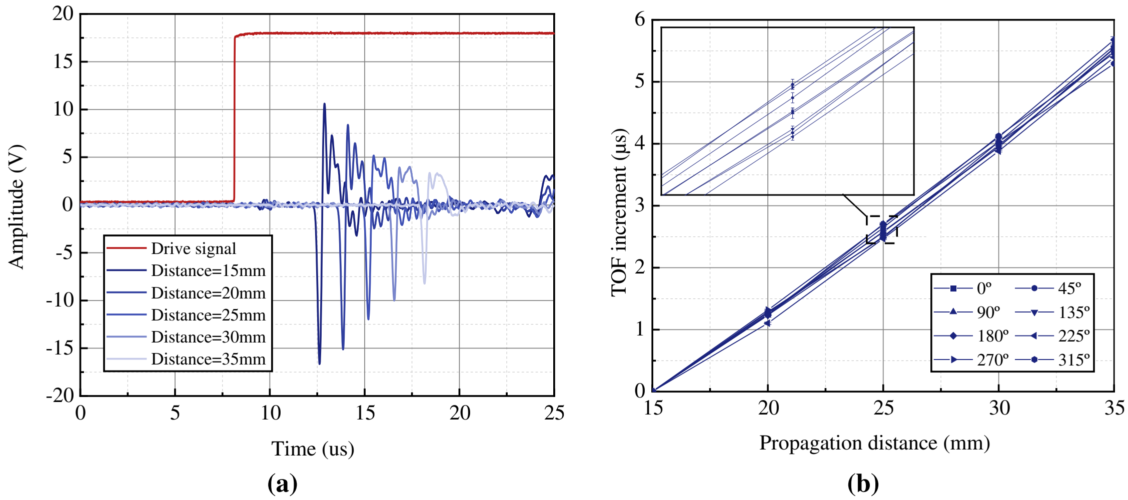

Figure 5: R-waves and TOF increments corresponding to specimen B28-1: (**a**) R-waves measured at different propagation distances on path B28-1-S1-0; (**b**) TOF increments corresponding to different paths on surface B28-1-S1.

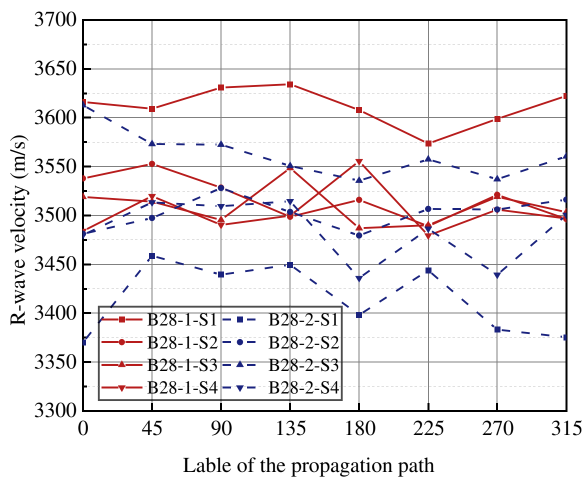

Figure 6: R-wave velocities measured along different propagation paths of specimens B28-1 and B28-2.

As expressed in Eq. (6), the evaluation of concrete stress requires determining the R-wave velocity in the stress-free state. For in-service concrete structures, the principal compressive stress direction can be easily determined. Therefore, the R-wave velocity measured near the testing point along a path perpendicular to the principal compressive stress direction can be approximated as the velocity in the stress-free state. This approximation is supported by two reasons. First, the surface concrete near the testing point has similar physical properties and stress-free R-wave velocities. Second, the R-wave velocity is insensitive to the compressive stress when the propagation path is perpendicular to the stress direction [29]. Consequently, the approximate R-wave velocity in the stress-free state of in-service concrete structures can be determined.

4.3 Influence of Stress and Stress History on the R-Wave Velocity

4.3.1 Influence of Stress on the R-Wave Velocity

After measuring the initial R-wave velocity in the stress-free state, cyclic loads were applied to Groups 3, 4, and 5. At each stress level, the R-wave velocity was measured. According to Eq. (6), the relative R-wave velocity was calculated to represent the velocity change. As shown in Fig. 7, the specimens, which were of the same age and had undergone similar loading procedures, exhibited different R-wave velocities at each stress level. This variation was attributed to the heterogeneity of the concrete. Despite these differences, for each specimen, the R-wave velocity varied cyclically with the cyclic load. When the load was applied, the R-wave velocity changed abruptly. However, this abrupt change did not affect the relationship between the wave velocity and the concrete stress.

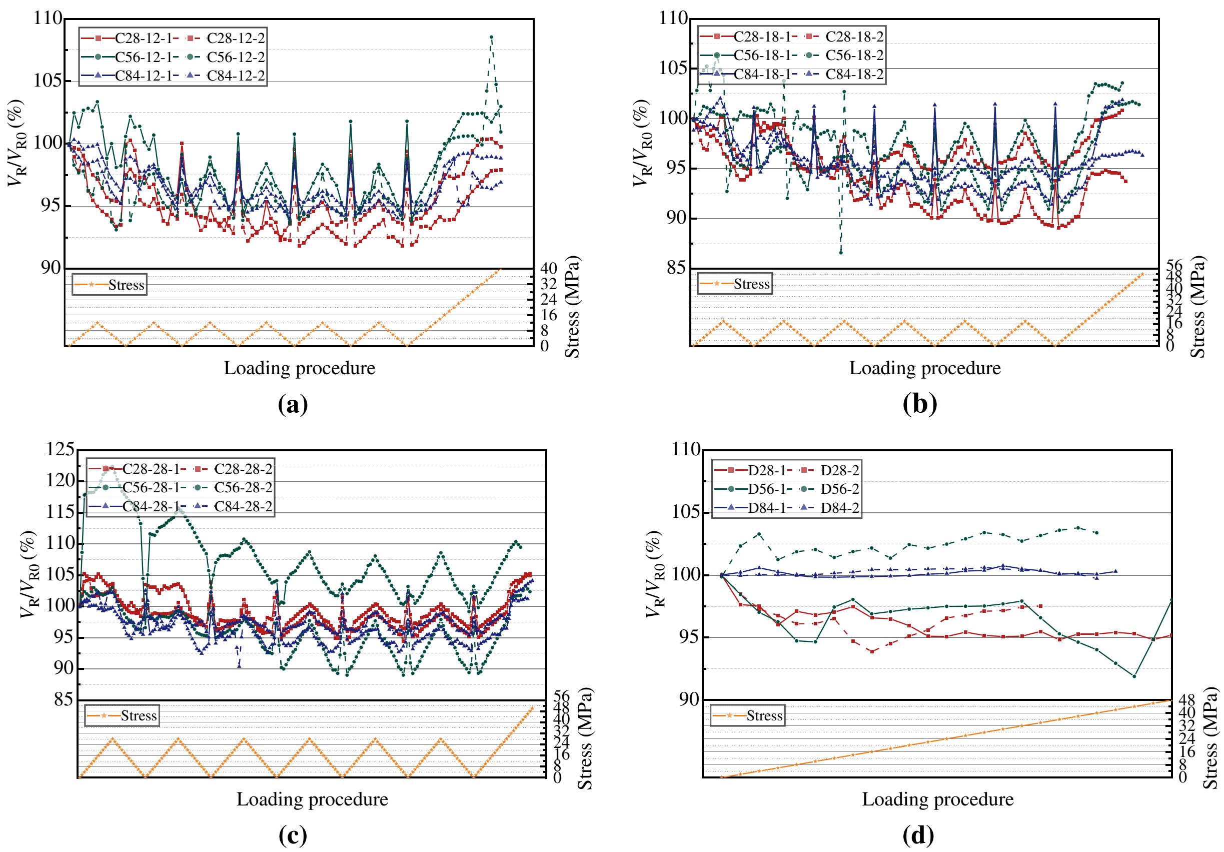

Figure 7: R-wave velocity and compressive stress varied with the cyclic load: (**a**) Results obtained from Group 3; (**b**) Results obtained from Group 4; (**c**) Results obtained from Group 5; (**d**) Results obtained from Group 6.

For Group 3, Cycles 1 and 2 induced the development of concrete defects and the changes in the microstructure, which masked the influence of stress on the R-wave velocity. Consequently, the R-wave velocity changed irregularly with the cyclic loading. Subject to the cyclic loading, the surface cracks and near-surface capillary porosity gradually closed. Since the cyclic load did not exceed the fatigue strength of the concrete, the development of defects and the changes in the microstructure ultimately reached a steady state. Beginning in Cycle 3, the R-wave velocity was proportional to the stress. The relative variation in R-wave velocity caused by stress was approximately 8%, while that caused by near-surface defects and the propagation medium was between 0.67% to 0.73%. This indicated that the heterogeneity of concrete would lead to a stress testing error ranging from 8.3% to 9.1%. In Cycle 7, the specimens were crushed. When the stress exceeded the historical stress, defects developed again. Although the R-wave velocity continued to increase with rising stress, it no longer exhibited a proportional relationship. As the concrete approached failure, the defects developed significantly. When defects were present along the propagation path, the increase in TOF due to defect development outweighed the increase in R-wave velocity caused by stress. This led to a decrease in the measured R-wave velocity.

Group 4 had similar results to Group 3. After Cycle 3, the proportional relationship between the R-wave velocity and the stress became evident. For Group 5, the applied load exceeded the fatigue strength. Due to the limited number of load cycles, no fatigue damage occurred. Consequently, the proportional relationship was also observed. Group 6, without preloading, was directly compressed to failure. The influences of the defect development and the increasing stress were coupled, resulting in irregular changes in the R-wave velocity. These experimental results demonstrate that the proposed stress testing method is applicable to in-service structures.

To further analyze the relationship between the R-wave velocity and the stress, the experimental results of specimen C28-12-1 are detailed in Fig. 8. Compared to Group 2, the R-wave signals collected from specimen C28-12-1 exhibited lower stability due to the universal testing machine. Unlike contact ultrasonic transducers, the relative position between the vibrometer and the specimen was variable. The specimen vibrated due to the vibration of the universal testing machine. As a result, the collection laser could not be fixed precisely at the collection point. Thus, the R-wave signals were collected 36 times and averaged to reduce errors. As shown in Fig. 8, a proportional relationship between the R-wave velocity and the stress was observed since Cycle 5. The R-wave measured at 2 MPa exhibited a significant delay compared to that at 0 MPa. Furthermore, as the stress exceeded 2 MPa, the R-wave shifted leftward as the stress increased. The TOF of the R-wave decreased, while the wave velocity increased. Because the measured R-waves were not identical, the TOF of the R-waves should be calculated using the cross-correlation method.

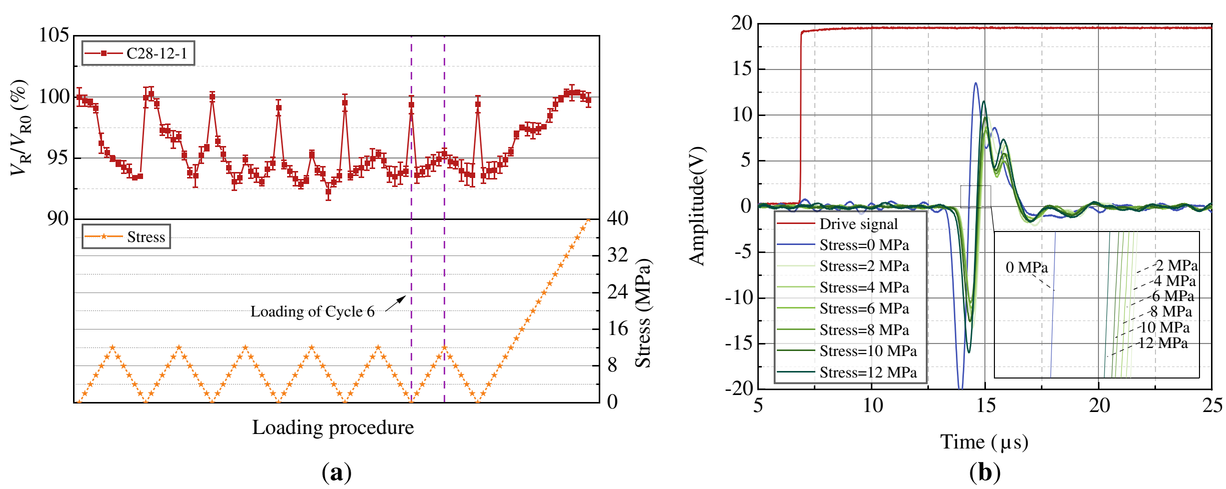

Figure 8: Experimental results of specimen C28-12-1: (**a**) R-wave velocity varied with stress; (**b**) R-waves measured in the loading stage of Cycle 6.

4.3.2 Influence of Stress History on the R-Wave Velocity

To analyze the influence of stress history on the R-wave velocity, Fig. 8a was converted into Fig. 9a. At the same stress level, the R-wave velocity varied with the number of load cycles, indicating that no plastic deformation occurred during Cycles 1 and 2. At the end of Cycle 3, the R-wave velocity decreased, indicating that plastic deformation occurred during Cycle 3. In subsequent load cycles, the R-wave velocity measured at the end of each cycle remained constant. As the cyclic loading progressed, the stress-velocity curve corresponding to each load cycle shifted downward. Starting from Cycle 5, the concrete defects reached a stable state. When the stress did not exceed the historical maximum stress, the defects did not develop any further. Consequently, the stress-velocity curve no longer shifted downward, resulting in a stable stress-velocity relationship. This phenomenon can also be observed in Fig. 9b. With increasing load cycles, the development of defects caused changes in the R-wave velocity. In Cycle 1, the fluctuations in the R-wave velocity indicated the presence of elastic defects in the specimen. Beginning in Cycle 2, the velocity measured at each stress level decreased as the cyclic loading progressed. The rate of velocity decrease slowed and stabilized since Cycle 5. This stabilization indicated that, since Cycle 5, the specimens exhibited the Kaiser effect, which indicates that the acoustic properties of concrete remain stable when the applied stress is less than the historical maximum stress. After stabilization, except for 0 MPa, the R-wave velocity increased with increasing stress.

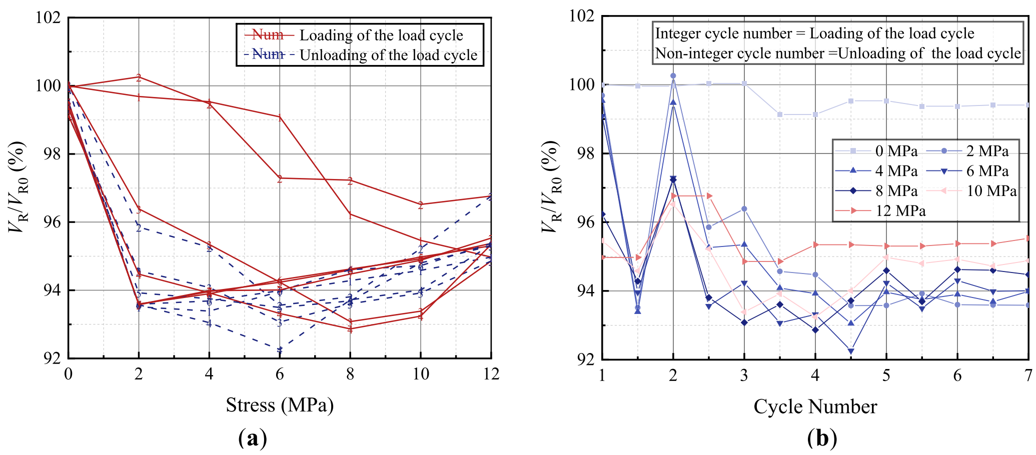

Figure 9: Influence of historical stress on the R-wave velocity of specimen C28-12-1: (**a**) Variation of the R-wave velocity with the stress; (**b**) Variation of the R-wave velocity with the cyclic load.

To evaluate the stress according to the measured R-wave velocity, linear fitting was performed on the measured R-wave velocity and stress. The data of Cycle 7 were from 2 MPa to the maximum stress of the cyclic load. The slope of the fitted line was the acoustoelastic coefficient of the specimens. The goodness of fit (R^2) was calculated to evaluate the linearity of the stress-velocity relationship. As shown in Fig. 10a, the acoustoelastic coefficients varied significantly during the early load cycles. This was due to the concrete not yet reaching a stable state. Consequently, the proportional relationship between the stress and the R-wave velocity was poor, resulting in a low R^2. As the number of load cycles increased, the acoustoelastic coefficient stabilized, and the R^2 began to rise. For Cycles 5, 6, and 7, the acoustoelastic coefficients ranged from 0.16 to 0.26, while the R^2 ranged from 0.57 to 0.99. The average acoustoelastic coefficient for these three cycles was 0.19, and the average R^2 was 0.85. This indicates that the influence of the maximum historical stress on the acoustoelastic coefficient is negligible.

Based on the acoustoelastic coefficient corresponding to the loading stage of Cycle 5 of specimen C28-12-1, the stress of each specimen was calculated using the measured R-wave velocity. The maximum stress applied to specimen C28-12-1 was 12 MPa, which was less than that applied to other specimens of the same group. This lower stress may have resulted in differences in the development of initial defects. As shown in Fig. 10a, the acoustoelastic coefficient used for the stress calculation was higher than that under other conditions.

Consequently, the calculated stress was generally lower than the actual stress, as shown in Fig. 10b. When the stress was less than 16 MPa, the stress testing error was less than 8 MPa. When the stress was greater than 16 MPa, the stress testing error was less than 2 MPa. This indicates that, after obtaining the acoustoelastic coefficient, the concrete stress can be evaluated using the R-wave velocity. In addition, the acoustoelastic coefficient can be determined by calibrating specimens with identical concrete mix designs. The aim is to improve the stress testing accuracy by minimizing the influence of the variation in the acoustoelastic coefficient [30].

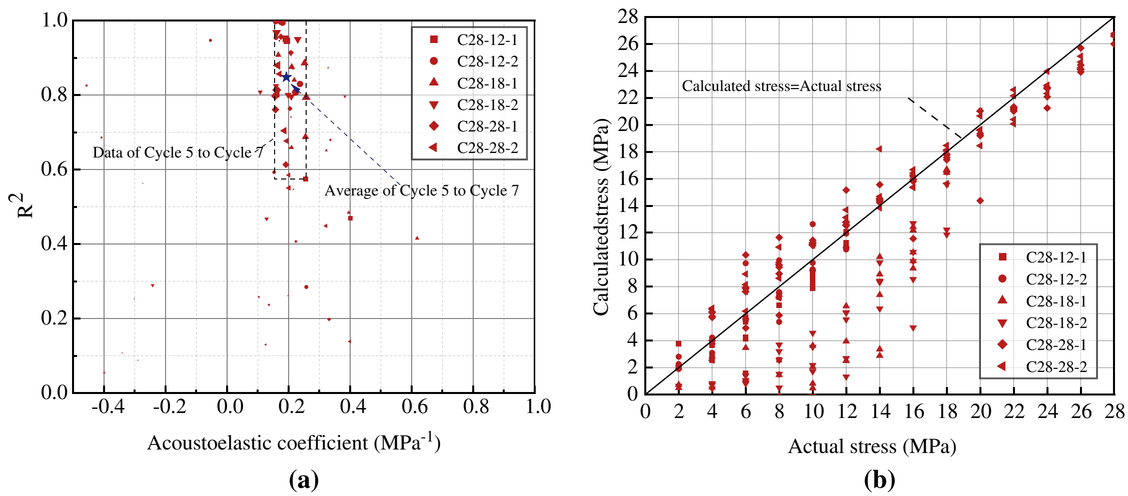

Figure 10: Acoustoelastic coefficient obtained by linear fitting and concrete stress calculated based on the R-wave velocity: (**a**) Acoustoelastic coefficients and R^2 (symbol size proportional to the number of load cycles); (**b**) Concrete stress calculated based on the acoustoelastic coefficient corresponding to the loading stage of Cycle 5 of specimen C28-12-1.

4.4 Influence of Concrete Age on Acoustoelastic Coefficients

As concrete ages, its physical properties change due to the progression of the hydration reaction, which in turn affects the acoustoelastic coefficient. To investigate the influence of concrete age on the acoustoelastic coefficient, the acoustoelastic coefficients corresponding to the specimens aged 56 and 84 days were calculated using the same methodology as for those aged 28 days. These calculations were based on data collected from Cycles 5 to 7 (except for 0 MPa). As shown in Fig. 11, the acoustoelastic coefficients corresponding to specimens of varying ages were different. Due to the heterogeneity of concrete, specimens of the same age also exhibited different acoustoelastic coefficients. For the specimens aged 56 days, the acoustoelastic coefficients ranged from 0.23 to 0.44 MPa^{-1}. For Cycles 5, 6, and 7, the average acoustoelastic coefficient was 0.36 MPa^{-1}, and the average R^2 was 0.91. For the specimens aged 84 days, the acoustoelastic coefficients ranged from 0.09 to 0.36 MPa^{-1}. For Cycles 5, 6, and 7, the average acoustoelastic coefficient was 0.15 MPa^{-1}, and the average R^2 was 0.91. The variation in the acoustoelastic coefficients among the specimens aged 28, 56, and 84 days indicates a correlation between the acoustoelastic coefficient and the concrete age.

The stress of the specimens aged 56 and 84 days was calculated based on the acoustoelastic coefficients corresponding to the loading stage of Cycle 5 of specimen C56-12-1 and C84-12-1, respectively. Due to the differences in the development of initial defects, the acoustoelastic coefficient used for the stress calculation was larger than that under other conditions. As a result, the calculated stress was generally lower than the actual stress. As shown in Fig. 12, for the specimens aged 56 days, the stress testing error was less than 8 MPa.

For the specimens aged 84 days, the stress testing error was relatively high when the stress exceeded 12 MPa. This high testing error was primarily attributed to the different stress histories of the specimens.

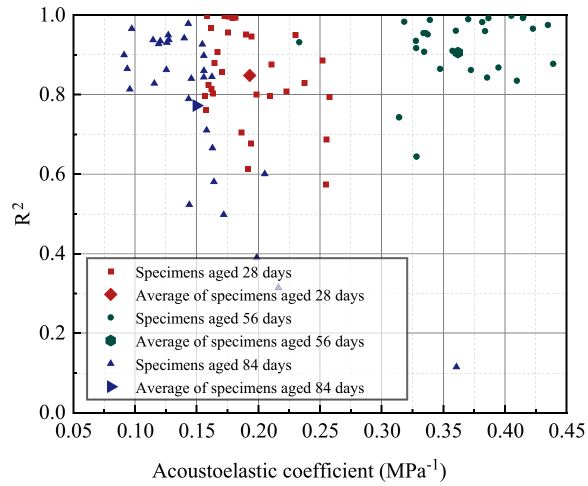

Figure 11: Acoustoelastic coefficient and R2 corresponding to specimens with different ages.

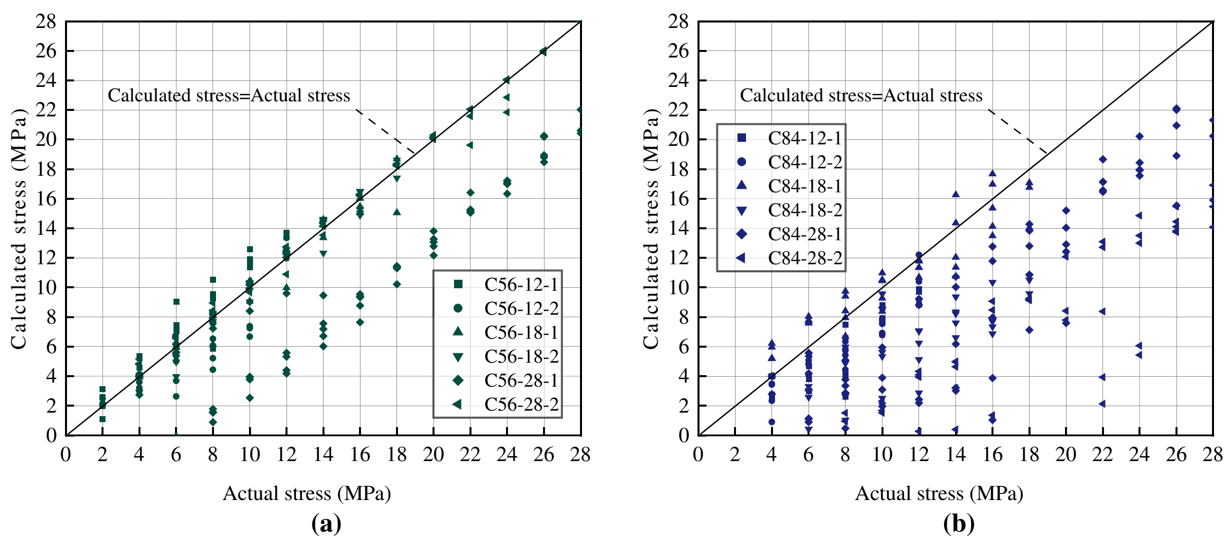

Figure 12: Concrete stress calculated based on the R-wave velocity: (**a**) Calculated stress of specimens aged 56 days; (**b**) Calculated stress of specimens aged 84 days.

The experimental results demonstrate that the acoustoelastic coefficient of the concrete varies with its age. Concrete specimens of the same age have similar acoustoelastic coefficients. Therefore, the acoustoelastic coefficient can be determined by calibrating reserved specimens or specimens extracted from in-service structures. Besides, the rate of change in concrete physical properties diminishes and stabilizes after a few years [31]. The acoustoelastic coefficient will also reach a stable state. Thus, for structures that have been in service for several years, the calibration of the acoustoelastic coefficient is required only once. Once the acoustoelastic coefficient is obtained, the concrete stress can be evaluated based on the measured R-wave velocity.

5 Conclusion and Future Work

In this paper, the laser ultrasonic technology was employed to test the concrete stress of in-service structures. A correlation model between the concrete stress and the R-wave velocity was established. Based on the theoretical analysis and the experimental results, a concrete stress evaluation method based on the R-wave velocity was proposed. The main conclusions are as follows:

(1) The R-wave velocity was influenced by the propagation medium, surface defects, and near-surface defects. On the same concrete surface, the R-wave velocity measured along a path perpendicular to the principal compressive stress can be approximated as the stress-free wave velocity. To reduce the stress testing error, the concrete surface along the testing path should be smooth and free of defects.

(2) Following a period of loading, the internal defects of the concrete reached a stable state, resulting in a stable acoustoelastic effect. The acoustoelastic coefficient can be determined by calibrating specimens with identical concrete mix designs. Once the acoustoelastic coefficient is obtained through linear fitting, the concrete stress can be evaluated using the R-wave velocity. When the stress was less or greater than 16 MPa, the testing error was less than 8 or 2 MPa, respectively.

(3) The acoustoelastic coefficient of concrete varied with age, but stabilized after a few years. For in-service structures, the concrete is subjected to cyclic loading induced by variable loads and the environment. The influence of stress history on the acoustoelastic coefficient has reached a stable state. In this condition, the acoustoelastic coefficient can be obtained through the calibration of reserved specimens or specimens extracted from in-service structures. Subsequently, the concrete stress can be calculated based on the velocity of the laser-generated R-wave. This method offers a promising solution for non-contact stress testing of in-service concrete structures.

The concrete age of the specimens used in this study was no more than 84 days, and their concrete mix designs were identical. To enhance the applicability of the proposed method, future work will investigate the long-term evolution of the acoustoelastic coefficient with concrete age. In addition, the influence of concrete mix design and heterogeneity on the acoustoelastic coefficient should be clarified. Such investigations could be conducted by combining experimental studies, numerical simulations, and machine learning algorithms.

Acknowledgement: Not applicable.

Funding Statement: This research was funded by the Research Program of Chongqing Institute of Urban Governance, grant number: 20240103.

Author Contributions: The authors confirm contribution to the paper as follows: Conceptualization, Mengxue Li and Xinyi Chen; methodology, Xinyi Chen; software, Mengxue Li; validation, Mengxue Li, Xinyi Chen and Yuxi Xie; investigation, Mengxue Li and Xinyi Chen; data curation, Xinyi Chen; writing—original draft preparation, Mengxue Li; writing—review and editing, Mengxue Li; funding acquisition, Mengxue Li. All authors reviewed and approved the final version of the manuscript.

Availability of Data and Materials: The data that support the findings of this study are available from the corresponding author, Xinyi Chen, upon reasonable request.

Ethics Approval: Not applicable.

Conflicts of Interest: The authors declare no conflicts of interest.

References

1. Kim TH. Analytical performance assessment of deteriorated prestressed concrete beams. Int J Concr Struct Mater. 2023;17(1):59. doi:10.1186/s40069-023-00624-1.

2. To DV, Sokoli D, Ghannoum WM, Moehle JP. Seismic performance of tall moment frames with high-strength reinforcement. ACI Struct J. 2021;118(1):113–24. doi:10.14359/51728180.
3. Shao Z, Shi L, Cai J. Wavelet modeling of signals for non-destructive testing of concretes. Meas Sci Technol. 2011;22(5):055702. doi:10.1088/0957-0233/22/5/055702.
4. Alam J, Neves LAC, Zhang H, Dias-da-Costa D. Assessment of remaining service life of deteriorated concrete bridges under imprecise probabilistic information. Mech Syst Signal Process. 2022;167:108565. doi:10.1016/j.ymssp.2021.108565.
5. Ghaedamini R, Ghassemi A, Atrian A. A comparative experimental study for determination of residual stress in laminated composites using ring core, incremental hole drilling, and slitting methods. Mater Res Express. 2019;6(2):025205. doi:10.1088/2053-1591/aaee46.
6. Wu J, Qiang B, Liao X, Huang Y, Yao C, Li Y. Hole-drilling method eccentricity error correction using a convolutional neural network. J Strain Anal Eng Des. 2023;58(2):118–29. doi:10.1177/03093247221080013.
7. Zhang T, Zhang L, Ozevin D, Attard T. Multi-scale ultrasonic imaging of sub-surface concrete defects. Meas Sci Technol. 2024;35(3):035901. doi:10.1088/1361-6501/ad128b.
8. Liu S, Wu C, Zhou J, Liu T, Zhuang S, Luo Y, et al. Relation between the shear stress distribution and the resulting acoustic emission variation in concrete beams. Struct Control Health Monit. 2020;27(6):e2528. doi:10.1002/stc.2528.
9. Yun H, Rayhana R, Pant S, Genest M, Liu Z. Nonlinear ultrasonic testing and data analytics for damage characterization: a review. Measurement. 2021;186:110155. doi:10.1016/j.measurement.2021.110155.
10. Ekin N, Uyanik O. Comparison of static and dynamic elastic moduli in concrete: effects of compressive strength, curing conditions and reinforcement. Iran J Sci Technol Trans Civ Eng. 2021;45(4):2327–43. doi:10.1007/s40996-020-00513-7.
11. Diewald F, Denolle M, Timothy JJ, Gehlen C. Impact of temperature and relative humidity variations on coda waves in concrete. Sci Rep. 2024;14(1):18861. doi:10.1038/s41598-024-69564-4.
12. Nogueira CL, Rens KL. Acoustoelastic response of concrete under uniaxial compression. ACI Mater J. 2019;116(3):21–33. doi:10.14359/51714462.
13. Zhong B, Zhu J, Morcous G. Measuring acoustoelastic coefficients for stress evaluation in concrete. Constr Build Mater. 2021;309:125127. doi:10.1016/j.conbuildmat.2021.125127.
14. Yu H, Lu L, Qiao P. Assessment of wave modulus of elasticity of concrete with surface-bonded piezoelectric transducers. Constr Build Mater. 2020;242:118033. doi:10.1016/j.conbuildmat.2020.118033.
15. Liang B, Li Z, Tao W, Wang Q, Yu Y, Zhai G. Giant magneto-acoustic transduction efficiency of a novel magnetostrictive-based electromagnetic acoustic transducer. Measurement. 2025;246:116720. doi:10.1016/j.measurement.2025.116720.
16. Li T, Zhang Y, Liu Y, Ma F, Wang W, Xu Z, et al. Research on unbonded defect imaging method of corrugated clad plate based on laser ultrasonics. Measurement. 2025;244:116485. doi:10.1016/j.measurement.2024.116485.
17. Wang C, Zhang F, Chen Y, Wang W, Wang Y, Lu K, et al. Study on the interaction mechanism of laser-generated Rayleigh waves and subsurface inclined cracks. Meas Sci Technol. 2024;35(11):115207. doi:10.1088/1361-6501/ad6787.
18. Park B, Sohn H, Liu P. Accelerated noncontact laser ultrasonic scanning for damage detection using combined binary search and compressed sensing. Mech Syst Signal Process. 2017;92:315–33. doi:10.1016/j.ymssp.2017.01.035.
19. Wang X, Wang Z, Ye Y. Rayleigh wave-based crack monitoring of mortar coating on prestressed concrete cylinder pipe under internal pressure. Constr Build Mater. 2024;442:137534. doi:10.1016/j.conbuildmat.2024.137534.
20. Feng Q, Zhong C, Qin L. Sandwich-type piezoelectric composite transducer for efficient heat dissipation. IEEE Sens J. 2024;24(7):10287–95. doi:10.1109/JSEN.2024.3366424.
21. Su J, Zhang P, Huang X, Pang X. Measurement method of stress in high-voltage cable accessories based on ultrasonic longitudinal wave attenuation. Sensors. 2024;24(17):5843. doi:10.3390/s24175843.
22. Philibert M, Yousry YM, Wong VK, Yao K. Ultrasonic surface wave transducers made of piezoelectric polylactic acid for structural health monitoring. IEEE Sens J. 2024;24(19):29770–7. doi:10.1109/JSEN.2024.3442307.

23. Duqennoy M, Ouaftouh M, Ourak M. Determination of stresses in aluminium alloy using optical detection of Rayleigh waves. Ultrasonics. 1999;37(5):365–72. doi:10.1016/S0041-624X(99)00009-8.
24. Breysse D. Nondestructive evaluation of concrete strength: an historical review and a new perspective by combining NDT methods. Constr Build Mater. 2012;33:139–63. doi:10.1016/j.conbuildmat.2011.12.103.
25. Gautam PK, Dwivedi R, Garg P, Majumder D, Agarwal S, McSaveney M, et al. Evolution of the damage precursor based on the felicity effect in shale. Int J Damage Mech. 2025;34(1):116–39. doi:10.1177/10567895241253727.
26. Rodríguez-Roblero MJ, Ayon JJ, Cascante G, Pandey MD, Alyousef R, Topper T. Application of correlation analysis techniques to surface wave testing for the evaluation of reinforced concrete structural elements. NDT E Int. 2019;102:68–76. doi:10.1016/j.ndteint.2018.11.003.
27. Xing J, Li F, Ma X, Qin Q. An optimal spatio-temporal hybrid model based on wavelet transform for early fault detection. Sensors. 2024;24(14):4736. doi:10.3390/s24144736.
28. Qian F, Xing G, Wang K, He L, Zhao B, Hu P, et al. Stress measurement by laser grating based on laser ultrasonic technology. Measurement. 2024;236:115049. doi:10.1016/j.measurement.2024.115049.
29. Niederleithinger E, Wolf J, Mielentz F, Wiggenhauser H, Pirskawetz S. Embedded ultrasonic transducers for active and passive concrete monitoring. Sensors. 2015;15(5):9756–72. doi:10.3390/s150509756.
30. Yang X, Chen L, Hao H, Yang Z, Ma B, Kong Q. Study on the dependence of the acoustoelastic effect in concrete on material strength. J Mater Civ Eng. 2024;36(11):04024354. doi:10.1061/jmcee7.mteng-18530.
31. Bompan KF, Haach VG. Ultrasonic tests in the evaluation of the stress level in concrete prisms based on the acoustoelasticity. Constr Build Mater. 2018;162:740–50. doi:10.1016/j.conbuildmat.2017.11.153.